Physics of the Earth and Planetary Interiors 172 (2009) 210–224

Contents lists available at ScienceDirect

Physics of the Earth and Planetary Interiors

journal homepage: www.elsevier.com/locate/pepi

Upwellings from a deep mantle reservoir filtered at the 660 km phase transition in thermo-chemical convection models and implications for intra-plate volcanism

J.R.G. van Summeren[a,*], A.P. van den Berg[a], R.D. van der Hilst[b]

[a] Utrecht University, Faculty of Earth Sciences, Budapestlaan 4, Utrecht 3584CD, The Netherlands
[b] Department of Earth, Atmospheric, and Planetary Sciences, Massachusetts Institute of Technology, 77 Massachusetts Avenue, Cambridge, MA 02139, USA

ARTICLE INFO

Article history:
Received 24 December 2007
Received in revised form 26 June 2008
Accepted 11 September 2008

Keywords:
Thermo-chemical convection
Mantle upwellings
Excess temperature
Transition zone
Intra-plate volcanism

ABSTRACT

With numerical modelling experiments we examine the influence of the 660 km post-spinel phase transition on the excess temperatures in and transport of compositional heterogeneity by deep mantle upwellings. We test our results against available observations on ocean island basalts (OIB). The endothermic post-spinel transition can cause localised, transient layering of convective flow in the upper mantle transition zone. Upwellings from the lower mantle, in our models the passive (mechanically driven) return flow from active (buoyancy-driven) downwellings, can transport heterogeneous material from deep mantle reservoirs across the transition zone into the upper mantle, but the phase transition can act as a chemical filter that can (locally) retain intrinsically denser elements in the lower mantle. A compositionally heterogeneous signature in upwellings from the lower mantle (e.g. Hofmann, A.W., 1997. Mantle geochemistry: the message from oceanic volcanism. Nature 385, 219–229) that is consistent with chemical diversity in OIB can be produced for a wide range of mantle evolution scenarios and stability conditions of compositional heterogeneity in the lower mantle. We demonstrate that the excess temperature in upwellings crossing the phase boundary increases with the background temperature contrast across the endothermic phase transformation, which itself increases with the degree of convective layering. For cases with a low degree of layering at the transition zone, the combination of upwellings of mid-mantle origin and intrinsically hot, deep-seated upwellings produce model results consistent with the formation of hotspots and large igneous provinces (LIP) at the surface. For high degrees of convective layering, however, lower mantle upwellings of high excess temperature would generate (with high frequency) massive flood basalt events. In view of the strong influence of transition zone convective layering on excess temperatures, the observed intra-plate volcanism in modern Earth suggests that on a global scale the degree of layering at the transition zone is low, which requires a low Clapeyron slope magnitude of the post-spinel phase transition. Because hot intrinsically dense material residing below the phase transition favours a high degree of convective layering, the Clapeyron slope magnitude must be even lower for this case in order to produce results consistent with inferences from mantle petrology.

1. Introduction

The scale and nature of convective upwelling relates to two long-standing, unresolved questions in mantle dynamics: the origin of intra-plate volcanism and the degree of convective layering at the transition zone. There is no consensus on whether intra-plate volcanism, such as large igneous provinces (LIP), hotspots, and seamounts have their origin in the upper or lower mantle (e.g. Campbell, 2007). Seismological evidence for the origin of mantle upwellings underneath hotspots is still ambiguous (e.g. Bijwaard and Spakman, 1999; Nataf, 2000; Nolet et al., 2006; Anderson, 2006).

If upwellings rising from the lower mantle are responsible for intra-plate volcanism, they must be consistent with surface observables. Isotope and trace-element geochemistry shows a heterogeneous chemical signature in ocean island basalts (OIB) compared to the more homogeneous mid-oceanic ridge basalts (MORB) (e.g. Hofmann, 1997). Thermo-chemical mantle convection (e.g. Christensen and Hofmann, 1994; Kellogg et al., 1999; Samuel and Farnetani, 2003; Xie and Tackley, 2004; Tan and Gurnis, 2007) provides a mechanism for producing OIB-like chemical signatures

---

* Corresponding author. Tel.: +31 30 2535076; fax: +31 30 2535030.
E-mail address: summeren@geo.uu.nl (J.R.G. van Summeren).

0031-9201/$ – see front matter © 2008 Elsevier B.V. All rights reserved.
doi:10.1016/j.pepi.2008.09.011

by assuming entrainment of chemically distinct material from largely isolated lower mantle reservoirs. Apart from geochemical arguments, the existence of compositionally distinct reservoirs in the deep mantle is supported by seismological evidence (e.g. Van der Hilst and Kárason, 1999; Ishii and Tromp, 1999; Saltzer et al., 2001, 2004; Trampert and van der Hilst, 2005; Deschamps et al., 2007; Kellogg et al., 2007). Furthermore, heat-producing elements and compositionally distinct material stored in the deep reservoir can complement Earth's heat budget and resolve apparent conflicts in istope systematics (e.g. Kellogg et al., 1999; Tolstikhin and Hofmann, 2005; Tolstikhin et al., 2006). An increase of the radiogenic heat production rate is expected when basaltic material associated with former subducted crust is concentrated in the compositionally distinct reservoir (e.g. Christensen and Hofmann, 1994; Kellogg et al., 1999; Nakagawa and Tackley, 2004; Van Thienen et al., 2005).

Upwellings that cause intra-plate volcanism also put constraints on excess temperature. The potential mantle temperatures (i.e. the temperature extrapolated to the surface along a mantle adiabat) can be inferred from the melting conditions of intra-plate volcanism caused by upwellings, which – in turn – is constrained by basalt geochemistry. An excess of 150–300 K of the potential temperature is estimated for intra-plate volcanism in comparison to MORB (e.g. Schilling, 1991; Putirka et al., 2007; Herzberg et al., 2007). Much larger excess temperatures would be expected, however, in upwellings originating from the core mantle boundary (CMB), for which a temperature contrast exceeding 1000 K is inferred (e.g. Boehler, 2000; Van der Hilst et al., 2007). It has been argued that a relatively small amount of cooling of mantle upwellings results from heat diffusion, adiabatic decompression, and thermal entrainment of surrounding (colder) mantle material (see e.g. Farnetani, 1997). Therefore, mechanisms must exist to lower the excess temperatures to sufficiently small values. Candidate mechanisms are upwellings originating at the top of a thermo-chemical boundary layer (Farnetani, 1997) and a sub-adiabatic temperature profile related to internal heating (Jeanloz and Morris, 1987; Bunge, 2005; Zhong, 2006).

The thermal evolution of mantle upwellings is influenced by the degree of mantle flow layering at the mantle transition zone between 410 and 660 km depth. Important dynamical implications are expected from the spinel → perovskite transition around 660 km depth, which is associated with a density increase of around 8–10% (Dziewonski and Anderson, 1981; Hirose, 2002) and a Clapeyron slope γ around -1 to $-3\,\mathrm{MPa\,K^{-1}}$ (e.g. Ito and Takahashi, 1989; Weidner and Wang, 1998; Hirose, 2002; Fei et al., 2004; Jacobs and de Jong, 2007). The endothermic phase transition acts as a barrier to convective flow (Olson and Yuen, 1982). The conditions for convective layering at the endothermic phase transition are expressed by the critical value for the dimensionless phase buoyancy parameter P, which depends linearly on the Clapeyron slope γ (see Table 1 for definition). Christensen and Yuen (1984, 1985) and Nakakuki et al. (1994) determined a critical value of around $P_{\mathrm{crit}} = -0.25$, which corresponds to a Clapeyron slope of $-3\ \mathrm{MPa\,K^{-1}}$ in our models. Around the critical value, local intermittent mixing between the upper and the lower mantle emerges, with alternating periods of layered and whole mantle convection (e.g. Machetel and Weber, 1991).

A partial barrier is compatible with seismological evidence showing that some subducting slabs and mantle upwellings cross the transition zone seemingly undisturbed, but perhaps with advective thickening (Fischer et al., 1988; Ribe et al., 2007), whereas others are deflected at this boundary (e.g. Van der Hilst et al., 1991, 1997; Fukao et al., 1999; Nolet et al., 2006). Although the resolution of structure associated with mantle upwelling is lower than for downwellings, a similar partial layering of upwellings is in agreement with seismological data. Recent studies suggest a large global variation in the connectivity of seismic velocity anomalies across the mantle transition zone, where a deep mantle origin has been suggested for only a part of the hotspot regions (e.g. Bijwaard and Spakman, 1999; Nolet et al., 2006, 2007; Zhao, 2007).

Weinstein (1992) demonstrated that the endothermic phase transition can filter mantle upwellings chemically, by preferentially restricting intrinsically dense material to the lower mantle, thereby inducing a compositional contrast across the phase transition. Similar chemical filtering affects downwellings, e.g. by separating the harzburgitic and basaltic fractions of a subducting slab (e.g. Mambole and Fleitout, 2002). For a pyrolite composition a density cross-over is inferred at the base of the mantle transition zone (Irifune and Ringwood, 1993; Ono et al., 2001), which induces chemical stratification – with harzburgite underlying MORB material – that contributes to convective layering at the phase transition (Irifune and Ringwood, 1993; Van Keken et al., 1996; Xie and Tackley, 2004; Nakagawa and Buffett, 2005). Without the effects of phase transitions, the critical density contrast for two-layer flow is estimated at 1–3% between the upper and lower mantle (Christensen, 1989; Kellogg, 1991; Nakakuki et al., 1994).

Clearly, the post-spinel phase transition is critical in controlling material exchange between the upper and lower mantle. Unfortunately however, the degree of convective layering is not fully constrained. The emphasis of previous work has been on investigating conditions for convective layering in relation to the endothermic post-spinel phase boundary and the influence of a compositional density contrast. In the present study the objective is to constrain the conditions under which upwellings from the deep mantle show Earth-like characteristics. We investigate the transport characteristics of thermo-chemical upwellings associated with a compositionally distinct reservoir in the lower mantle, and we test model predictions against observed intra-plate volcanism (notably ocean–island basalts). Specifically, we analyse the thermal and compositional expression of material entering the upper mantle from below along with constraints from mantle petrology. We focus on models that exhibit weak layering due to the 660 km phase boundary, in line with observational evidence and include Clapeyron slope values ranging from -1.25 to $-2.5\,\mathrm{MPa\,K^{-1}}$, in line with current petrological uncertainties. As far as we are aware, the influence of the post-spinel phase transition on increasing the excess temperature of upwellings has not been systematically investigated before. We show that upwellings of lower mantle origin are compositionally heterogeneous for a large range of possible thermo-chemical convection scenarios (e.g. Kellogg et al., 1999; Becker et al., 1999; Hansen and Yuen, 2000; Tackley, 2002) and that excess temperatures in upwellings correpond to petrological estimates for specific degrees of convective layering and stability of a compositionally distinct deep mantle reservoir.

2. Methods used in numerical modelling

We examine thermo-chemical mantle convection through numerical experiments that simulate an incompressible linearly viscous fluid at infinite Prandtl number. For the numerical convection model, we use the following extended-Boussinesq formulation (e.g. Christensen and Yuen, 1985; Steinbach et al., 1989; Ita and King, 1994):

$$\partial_j u_j = 0 \tag{1}$$

$$-\partial_i\,\Delta P + \partial_j \tau_{ij} = (\alpha(z) Ra T - Rb_{\mathrm{ph}} \Gamma_{\mathrm{ph}} - Rb_{\mathrm{C}} C)\delta_{i3} \tag{2}$$

$$\tau_{ij} = \eta(T, P)(\partial_j u_i + \partial_i u_j) \tag{3}$$

$$\frac{DT}{Dt} = \partial_j \partial_j T + \alpha(z) Di u_z (T + T_0) + \gamma \frac{Rb_{\mathrm{ph}}}{Ra} Di \frac{D\Gamma_{\mathrm{ph}}}{Dt}(T + T_0)$$

Table 1
Symbol definitions and parameter values.

Symbol	Property	Value	Dimension
γ	Clapeyron slope		MPa K^{-1}
$\Gamma_{\mathrm{ph}} = \frac{1}{2}\left(1 + \sin\left(\pi \frac{z - z_{\mathrm{ph}}}{2d_{\mathrm{ph}}}\right)\right)$	Phase parameter		–
d_{ph}	Phase transition halfwidth	50	km
$\frac{\delta\rho_{\mathrm{ph}}}{\rho_0}$	Phase density contrast	0.1	–
T_{ph}	Reference temperature phase transition	2073	K
P_{ph}	Reference pressure phase transition	2.97×10^{10}	Pa
C	Composition parameter		–
$\frac{\delta\rho_{\mathrm{C}}}{\rho_0}$	Compositional density contrast		–
ΔT	Temperature scale	3727	K
T	In situ temperature		K
T_{S}	Surface temperature	273	K
T^0_{CMB}	Initial core temperature	4000	K
T_{bg}	Background temperature		K
$T_{\mathrm{ex}} = T - T_{\mathrm{bg}}$	Excess temperature		K
t	Model time		s
ρ	Density		kg m^{-3}
ρ_0	Density scale	4500	kg m^{-3}
ΔP	Dynamic pressure		Pa
c_{P}	Specific heat	1.25×10^3	J kg^{-1} K^{-1}
g	Gravitational acceleration	10	m s^{-2}
h	Mantle depth	2.9×10^6	m
k	Thermal conductivity	5	W m^{-1} K^{-1}
$\kappa = \frac{k}{\rho c_{\mathrm{P}}}$	Thermal diffusivity		m^2 s^{-1}
$\Phi = \eta e^2$	Viscous dissipation function		–
$e = \left(\frac{1}{2} e_{ij} e_{ij}\right)^{1/2}$	Second invariant strain rate tensor		s^{-1}
u	Convective flow velocity		m s^{-1}
$\tau = \eta e_{ij}$	Viscous stress tensor		Pa
$Ra = \frac{\rho_0 \alpha_0 g\, \Delta T h^3}{\kappa_0 \eta_0}$	Rayleigh number	1.9×10^8	–
$Rb_{\mathrm{C}} = \frac{\delta\rho_{\mathrm{C}} g h^3}{\eta_0 \kappa_0}$	Compositional Rayleigh number		–
$Rb_{\mathrm{ph}} = \frac{\delta\rho_{\mathrm{ph}} g h^3}{\eta_0 \kappa_0}$	Phase Rayleigh number	2.47×10^8	–
$Di = \frac{\alpha_0 g h}{c_{\mathrm{P}}}$	Dissipation number	0.46	–
$R = \frac{H_0 h^2}{c_{\mathrm{P}} \kappa_0\, \Delta T}$	Internal heating number	32.9	–
$H(t) = H_0 \exp\left(\frac{-\ln(2) t}{\tau_{1/2}}\right)$	Time-dependent internal heating		W kg^{-1}
H_0	Initial internal heat production	17.411×10^{-12}	W kg^{-1}
$\tau_{1/2}$	Radioactive half-life time	2.5×10^9	year
$P = \frac{\gamma \delta\rho_{\mathrm{ph}}}{\rho_0^2 \alpha_0 g_0 h}$	Phase boundary buoyancy parameter		–
$B = \frac{\delta\rho_{\mathrm{C}}}{\rho_0 \alpha_0\, \Delta T}$	Compositional buoyancy number		–
$\alpha(z) = \frac{\alpha_0\, \Delta\alpha}{((\Delta\alpha^{1/3} - 1)(1 - z) + 1)^3}$	Thermal expansivity		K^{-1}
α_0	Thermal expansivity scale	2×10^{-5}	K^{-1}
$\Delta\alpha$	Thermal expansivity contrast	0.2	–
$\eta(T, z) = \eta_0 \exp(\Delta\eta_{\mathrm{P}} z - \Delta\eta_T T)$	Dynamic viscosity		Pa s
η_0	Viscosity scale	5×10^{20}	Pa s
$\Delta\eta_{\mathrm{P}}$	Pressure related viscosity contrast	20	–
$\Delta\eta_T$	Temperature related viscosity contrast	100	–
M_{tot}	Total mass transport rate		s^{-1}
M_{het}	Heterogeneous mass transport rate		s^{-1}
f_{het}	Fractional heterogeneity of mass transport		–

$$+\frac{Di}{Ra}\Phi + RH(t) \tag{4}$$

$$\frac{DC}{Dt} = \frac{\partial C}{\partial t} + u_j \partial_j C = 0 \tag{5}$$

Symbols used are explained in Table 1. Mass conservation of the incompressible fluid model is expressed in the continuity Eq. (1). The Stokes Eq. (2) describes the conservation of momentum, assuming an infinite Prandtl number. The constitutive Eq. (3) defines a linear viscous rheology dependent on temperature and pressure. The energy Eq. (4) describes heat transport, where the right-hand side terms are for heat diffusion, adiabatic heating, latent heat of the phase transition, viscous dissipation, and radiogenic internal heating, respectively. The advection equation for composition (5) describes transport of compositional hetero-

Table 2
Key parameters for the models investigated and temperature changes during phase crossing.

Model	γ (MPa K^{-1})	$\frac{\delta\rho_C}{\rho_0}$ (%)	Figure	$\bar{\delta}T_{ex}$	$\bar{\delta}T_{bg}$	$\bar{\delta}T$	P_e	B_e
S00	−2.50	0	–	55 ± 40	-68 ± 36	-13 ± 24	−0.178	0.
S09	−2.50	0.9	Fig. 1 a and b	61 ± 38	-74 ± 28	-13 ± 26	−0.178	0.225
S14	−2.50	1.4	Fig. 1 c and d	82 ± 54	-97 ± 48	-16 ± 27	−0.178	0.349
S20	−2.50	2	Fig. 1 e and f	98 ± 67	-109 ± 52	-11 ± 33	−0.178	0.497
H10	−2.50	1.4	–	96 ± 44	-110 ± 22	-14 ± 33	−0.178	0.349
W09	−1.25	0.9	Fig. 2 a and b	19 ± 27	-29 ± 23	-9 ± 17	−0.0889	0.225
W14	−1.25	1.4	Fig. 2 c and d	2 ± 16	-8 ± 8	-7 ± 13	−0.0889	0.349
W20	−1.25	2	Fig. 2 e and f	23 ± 30	-32 ± 25	-9 ± 16	−0.0889	0.497

See Sections 2.1 and 3.3 for explanation of symbols. The average temperature values and variance is given for the tracers that have crossed the phase transition boundary during the model time interval 3.6–4.5 Gyr.

geneities by means of convective flow — diffusion of material is excluded. In our models, thermal expansion decreases with increasing pressure, which stabilises dense heterogeneous material at the bottom of the mantle and which reduces the critical density contrast for stability of such heterogeneities (Hansen and Yuen, 2000).

In our models, buoyancy variations that drive convection depend on variations in temperature, mineral phase, and chemical composition, as described by the following equation of state:

$$\rho = \rho_0 \left(1 - \alpha(z)(T - T_S) + \Gamma_{ph}\frac{\delta\rho_{ph}}{\rho_0} + C\frac{\delta\rho_C}{\rho_0} \right) \tag{6}$$

The convection Eqs. (1)–(6) are solved using the SEPRAN finite element package (Van den Berg et al., 1993; Segal and Praagman, 2000). In order to model the non-diffusive composition field, 1.2 million active particle tracers are advected with the convective flow using a 4th-order Runge–Kutta scheme. The tracers are used in a particle-in-cell interpolation (Hockney and Eastwood, 1988) in the evaluation of composition-dependent quantities, such as compositional density contrasts. We use a two-dimensional cylindrical shell of 180 degrees opening angle with a nodal point resolution between 5 and 23 km. A geometrical scaling of the mantle domain mimics the surface–volume characteristics of a 3D sphere that control the thermal evolution. Van Keken (2001) demonstrated that scaling of the inner-to-outer surface ratio is required to calculate the heat production and heat flow appropriately in a mantle that is heated from below. Because the mantle model that we consider is primarily heated from within, it is appropriate to rescale the volume-to-surface ratio for the cylindrical model, such that it approximates that of the spherical Earth. To this end, the inner and outer radii of the mantle are given the dimensionless values 0.3 and 1.3, respectively. A time window of 4.5 Gyr allows us to study the long-term evolution of Earth's mantle. We use time-dependent radio-active internal heating – uniformly distributed across the mantle (except for model H10) – that decays with a half-life time of 2.5 Gyr to an approximately chondritic value of 5×10^{-12} W kg^{-1} at the end of the model time of 4.5 Gyr.

Free slip, impermeable boundary conditions are prescribed on all sides, and reflecting temperature conditions are applied to the side boundaries. For the initial temperature we apply an adiabatic depth profile of potential temperature $T_P = 1960$ K, truncated at the top and bottom boundary layers. The surface temperature is kept constant at 273 K and the core temperature is put to 4000 K initially, and varies in time as a result of thermal coupling with a heat reservoir representing the core, as described in Van den Berg et al. (2005). A chemically dense reservoir is initially placed at the bottom 35 vol% of the mantle. Within this initial layer configuration the excess density varies linearly with the composition parameter C from zero at the top to a maximum value $\delta\rho_C/\rho_0$ at the bottom.

To model the solid-state post-spinel phase transition we use a negative Clapeyron slope γ and a density contrast of $(\delta\rho_{ph}/\rho_0) = 10\%$; both parameters promote convective layering at the phase transition (e.g. Turcotte and Schubert, 2002). For numerical reasons the halfwidth of the phase transformation is set to 50 km. We focus on the influence of the post-spinel phase transition and disregarded other phase transformations in the mantle. Numerical modelling (e.g. Solheim and Peltier, 1993) has demonstrated, however, that convective layering at the endothermic phase transition and the corresponding development of a thermal boundary reduces as a results of nearby exothermic phase changes (e.g. olivine → spinel near 410 km depth, ilmenite → perovskite near 660 km, and garnet-majorite to perovskite near 700 km in a mantle of pyrolite composition (e.g. Weidner and Wang, 1998)).

Viscosity varies exponentially with temperature and pressure by a factor of 100 and 20, respectively, in our model. Temperature-dependent viscosity tends to increase the propensity to layering and to focus upwellings in a low-viscosity zone underneath the phase transition (Steinbach and Yuen, 1995). A viscosity increasing with depth tends to stagnate and broaden the convective flow in the deep mantle (e.g. Hansen et al., 1993). The thermal expansivity across the mantle's depth range decreases by a factor of 5 across the mantle (Chopelas and Boehler, 1992; Steinbach and Yuen, 1994), which reduces the (positive) thermal buoyancy for a given temperature anomaly. A list of model parameters is given in Tables 1 and 2 including values for γ and $\delta\rho_C/\rho_0$ that are used as control parameters in the experiments.

2.1. Description of mass transport and excess temperature diagnostic

In order to monitor the thermal and chemical characteristics of upwellings at the post-spinel phase transition we use diagnostics based on passive particle tracers that are defined in addition to the set of active particle tracers mentioned above. A total of 2000 randomly distributed passive monitor tracers were used to monitor the local space coordinates, composition, and temperature at every integration time step of the model equations. The monitor data were used to analyse the impact of several model parameters on the transport of compositionally distinct reservoir material from the lower mantle into the upper mantle. Monitor tracers are diagnosed at 18 km above and below the phase transition. Within this depth range the phase parameter changes value from $\Gamma_{ph} = .05$ to .95. Monitor tracers in mantle upwellings that cross the observation depths above and below the phase transition are labeled with the superscripts 'um' and 'lm', respectively.

Using the monitor data, we calculate the rate of total mass transport across the two interfaces enclosing the phase transition, denoted M_{tot}^{um} and M_{tot}^{lm}. The statistical stability of the total mass transport was demonstrated by the convergence of M_{tot}^{lm} for an increasing number of monitor tracers, with a difference smaller than 1% between results calculated using 1000 and 2000 monitor tracers. The composition parameter C is evaluated for the n_{bin} monitor tracers that cross the interface during a time bin of length

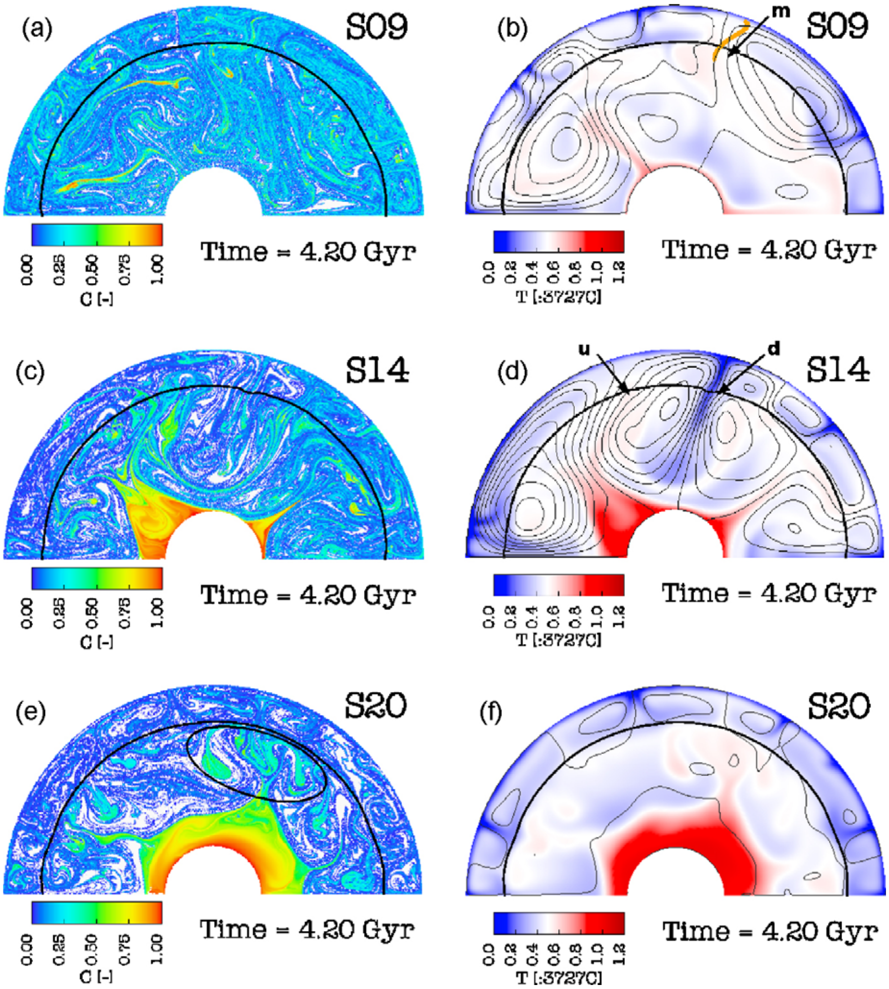

Fig. 1. The composition field is shown in frames a, c, and e. Frames b, d, and f show the temperature field and stream lines (thin black lines). Models shown are (a and b) S09 ($\delta\rho_C/\rho_0 = 0.9\%$), (c and d) S14 ($\delta\rho_C/\rho_0 = 1.4\%$), and (e and f) S20 ($\delta\rho_C/\rho_0 = 2.0\%$). The thick black line indicates the endothermic phase transition. The Clapeyron slope in the models is $\gamma = -2.5\,\mathrm{MPa\,K^{-1}}$. The arrow labeled 'm' in frame (b) shows a mid-mantle upwelling. The arrows labeled 'd' and 'u' in frame (d) show examples of an active, localised mantle downwelling, and a passive broad-scale mantle upwelling, respectively. The elliptic region in frame (e) shows an example of compositionally distinct material residing underneath the phase transition. The orange line in frame (b) indicates the monitor tracer path for which the monitored temperature is shown in Fig. 8 a. (For interpretation of the references to colour in this figure legend, the reader is referred to the web version of the article.)

Δt. The mass transport rate – in mantle masses per billion years – is defined as $M_{\mathrm{tot}} = (1/n_{\mathrm{pt}}\,\Delta t)\sum_{i=1}^{n_{\mathrm{bin}}}(1 + C_i(\delta\rho_C/\rho_0))$. n_{pt} is the total number of monitor tracers in the mantle domain. The injection rate for the excess mass of compositionally distinct material is calculated in a similar way by $M_{\mathrm{het}} = (1/n_{\mathrm{pt}}\,\Delta t)\sum_{i=1}^{n_{\mathrm{bin}}} C_i(\delta\rho_C/\rho_0)$. The ratio $f_{\mathrm{het}} = (M_{\mathrm{het}}/M_{\mathrm{tot}})$ measures the mass fraction of heterogeneous material injected into the upper mantle.

To calculate the excess temperature T_{ex} at the monitor tracers, the background temperature T_{bg}, based on the horizontally averaged geotherm, is subtracted from the absolute temperature: $T_{\mathrm{ex}} = T - T_{\mathrm{bg}}$. Hereinafter, the temperatures are 'in situ' values, unless mentioned otherwise (e.g. potential temperatures). Geochemically inferred excess temperatures of hotspots are relative to potential temperatures inferred underneath ridges, which lie outside cold regions of slab subduction. For a proper comparison to the observations we, therefore, exclude lower-than-average temperatures that are associated with downwellings in calculating T_{bg}. The excess temperature in upwellings is examined near the phase transition as defined above. Tracers that cross the upper and lower observation depths near the phase transition are labeled 'um' and 'lm', respectively. A change in T during phase boundary crossing is defined as $\delta T = T^{\mathrm{um}} - T^{\mathrm{lm}}$. In addition to monitoring at phase transition depth, excess temperatures are calculated at 300 km depth, for comparison with geochemically inferred excess temperatures. Using a 'sub-lithospheric' depth of 300 km ensures that thermal effects of the surface thermal boundary layer are excluded. Because the geochemical estimates are derived from surface potential temperatures, it is important to understand how the excess temperatures are affected when extrapolated to 300 km depth. For the applied mantle parameterisation, the excess of in situ temperatures is 4% larger at 300 km than at the surface. Thus, when compared to an excess of potential temperatures, typical values for T_{ex} of 250 K calculated from our models, are overestimated by a value of around 10 K. This small difference allows for a comparison between calculated excess temperatures calculated in the numerical modelling experiments and petrological estimates of the excess temperatures.

3. Results

3.1. Evolution of thermo-chemical convection models

The behaviour of upwellings of lower mantle origin is determined by the parameterisation used in the mantle convection models. Key parameters are the maximum density contrast of the thermo-chemical reservoir $\delta\rho_C/\rho_0$ and the Clapeyron slope γ of the endothermic phase transition. Values for different models are listed in Table 2. Effective dimensionless parameters for the phase buoyancy $P_e = \gamma\delta\rho_{ph}/(\rho_0^2\langle\alpha\rangle g_0 h)$ and compositional buoyancy $B_e = \delta\rho_C/(\rho_0\langle\alpha\rangle\Delta T)$ are given for the initial condition, where the terms between $\langle\,\rangle$-brackets are average mantle values. The initial effective Rayleigh number is $Ra_e = 4 \times 10^6$.

The effect of $\delta\rho_C/\rho_0$ on the thermo-chemical reservoir configuration in the convecting mantle through time is investigated for models with a constant Clapeyron slope $\gamma = -2.5\,\mathrm{MPa\,K^{-1}}$. In Fig. 1, the composition and temperature field is shown after a model time of $t = 4.2$ Gyr. Fig. 1 a and b shows a thermo-chemical reservoir that is configured as stretched-out blobs dispersed throughout the mantle, which results from a low excess density contrast of $\delta\rho_C/\rho_0 = 0.9\%$ (model S09). Shown in Fig. 1 c and d is a reservoir that has evolved as isolated piles of dense material on top of the CMB, for $(\delta\rho_C/\rho_0) = 1.4\%$ in model S14. Fig. 1 e and f shows a thermo-chemical layer enclosing the CMB for $\delta\rho_C/\rho_0 = 2.0\%$ in model S20. Topography on the layer's interface is induced by overlying convective motion. Thus, progressively more stable reservoir configurations are observed for increasing values of the density contrast $\delta\rho_C/\rho_0$—a results that is consistent with other modelling studies (e.g. Kellogg et al., 1999; Becker et al., 1999; Tackley, 2002; Van Thienen et al., 2005).

The endothermic phase transition acts as a partial barrier to the convective flow and has important dynamical consequences. Fig. 1 shows an instant of largely layered mantle convection when slabs pond at the phase transition. These periods contrast with vigourous whole mantle convection that occur when the ponded material breaks through the phase boundary after reaching critical mass and sinks into the lower mantle, as shown in Fig. 1 d. As a consequence of the temporary deflection of subducting slabs at the phase transition – prior to sinking into the lower mantle – an intermittent style of mantle convection results (e.g. Machetel and Weber, 1991). Consistent with the results in e.g. Steinbach et al. (1993) and Tackley (1995), the intermittent style of convection in our models gradually weakens due to secular cooling of the upper mantle; downwellings are becoming larger and, thereby, less sensitive to deflection at the phase barrier.

The dynamics in our models is to a large extent controlled by active (buoyancy-driven), high-velocity, localised convective downwellings, of which an example is shown in Fig. 1 (arrow labeled 'd'). In general, downwellings induce a passive (mechanically driven) return flow across the phase transition in the form of low-velocity, broad-scale upwellings (arrow labeled 'u' in Fig. 1 d). Absent in our models are active mantle upwellings (plumes), caused by a boundary layer instability, often considered an important ingredient of mantle dynamics (e.g. Morgan, 1971; Campbell, 2007). Internal heating, depth-decreasing thermal expansivity, depth-increasing viscosity, and the presence of compositional anomalies tend to reduce the vigour of convection in the lowermost mantle (e.g. Davies, 1986; Hansen et al., 1993; Hansen and Yuen, 2000). As a consequence of the resistance to deep mantle convective flow, many downwellings are being recycled at intermediate mantle depths in our models. This is shown in Fig. 1 b, d, and f, where the cold temperature anomalies suggest that downwellings stagnate at progressively shallower depths in the lower mantle. A variable depth of subduction was proposed by Albarede and Van der Hilst (2002) as a mechanism to maintain a vertical concentration gradient in the mantle, which supports the preservation of chemically distinct reservoirs, without inducing seismic reflections or scattering at mid-lower mantle depths, for which seismological evidence is lacking (e.g. Castle and Van der Hilst, 2003). Fig. 1 shows a clear example of a reservoir with a radial compositional concentration gradient, that is maintained on a long time scale.

Fig. 1 c and d illustrates how cold downwellings destabilise a heterogeneous reservoir in the deep mantle. The upwellings that are triggered by this process do not rise towards the surface undisturbed, however. Deflection of these upwellings underneath the phase transition results in lateral material transport in the shallow lower mantle. As a result, passive upwellings have a source-region in the shallow lower mantle (see e.g. Fig. 1 b, arrow labeled 'm'). Cserepes and Yuen (2000) demonstrated that such upwellings can occur when the phase transition acts as a strong, but not complete barrier to the convective flow. Strong lateral variations in the composition field that form underneath the phase transition (see the elliptic region in Fig. 1 e) can reach the upper mantle by means of these passive mid-mantle upwellings. This way, the lower mantle is leaking heterogeneous material into the upper mantle, triggered by cold downwellings breaking through the phase boundary in a top-down dynamical setting.

Fig. 2 shows the results of similar experiments, but for a weaker phase boundary with a Clapeyron slope of $\gamma = -1.25\ \mathrm{MPa\,K^{-1}}$. Compared to Fig. 1, these models are characterised by a significant reduction in the deflection of up- and downwellings at the phase transition, due to the reduced magnitude of γ. As a consequence of the reduction in slab ponding at the transition zone, the convective vigour of downwellings that sink into the lower mantle is reduced. Associated to this are relatively low mantle flow velocities at downwelling events. This is further illustrated in Fig. 3, which shows time series of the root-mean-square mantle flow velocities (v_{RMS}). Regular v_{RMS} maxima in the left-hand frames correspond to flushing events (Machetel and Weber, 1991), where material ponding at the phase boundary has reached critical mass and breaks through the boundary. Peak velocities are lower and less localised in time in the models with a reduced Clapeyron slope (right-hand column). Another consequence of the smaller Clapeyron slope is that direct ascent of deep-seated upwellings into the upper mantle is promoted. An example of such an upwelling is shown in Fig. 2(elliptic region).

Characteristic time and length-scales for passive mid-mantle upwellings and active deep-seated upwellings are depicted for model W20 in Fig. 4. The in situ temperature is depicted as a function of the angular coordinate and model time at a depth of 300 and 1000 km. For the deep-seated upwelling, indicated by the arrow labeled 'ds', typical time-scale and length-scales are approximately 100 Myr and approximately 100 km, respectively. A high temperature anomaly is present at both depth levels, corresponding to a single upwelling originating from the deep mantle. Passive upwellings persist on a Gyr time-scale and extend over 1000s of km in lateral direction (located in between the blue regions that indicate cold downwellings). The thermal anomaly of these passive upwellings is much smaller and the connectivity to a depth of 1000 km is weaker than for the deep-seated upwellings.

The degree of decoupling of the convective flow across the endothermic phase transition is illustrated by the time-averaged depth profiles of the radial flow velocity, background temperature, and the composition parameter in Fig. 5. For the models with the larger Clapeyron slope magnitude, increased convective layering is indicated by the drop in radial flow velocity (frame a and d). As a result, a temperature contrast of several hundred degree between the upper and lower mantle evolves, in line with previous modelling studies of e.g. Tackley et al. (1993). For the models with a smaller Clapeyron slope magnitude the temperature contrast is less than 100 K (frame e). The curves in frame b and e show an increase of the temperature constrast across the phase transition associated with convective layering for larger values of the compositional excess density, because intrinsically dense material is more likely to

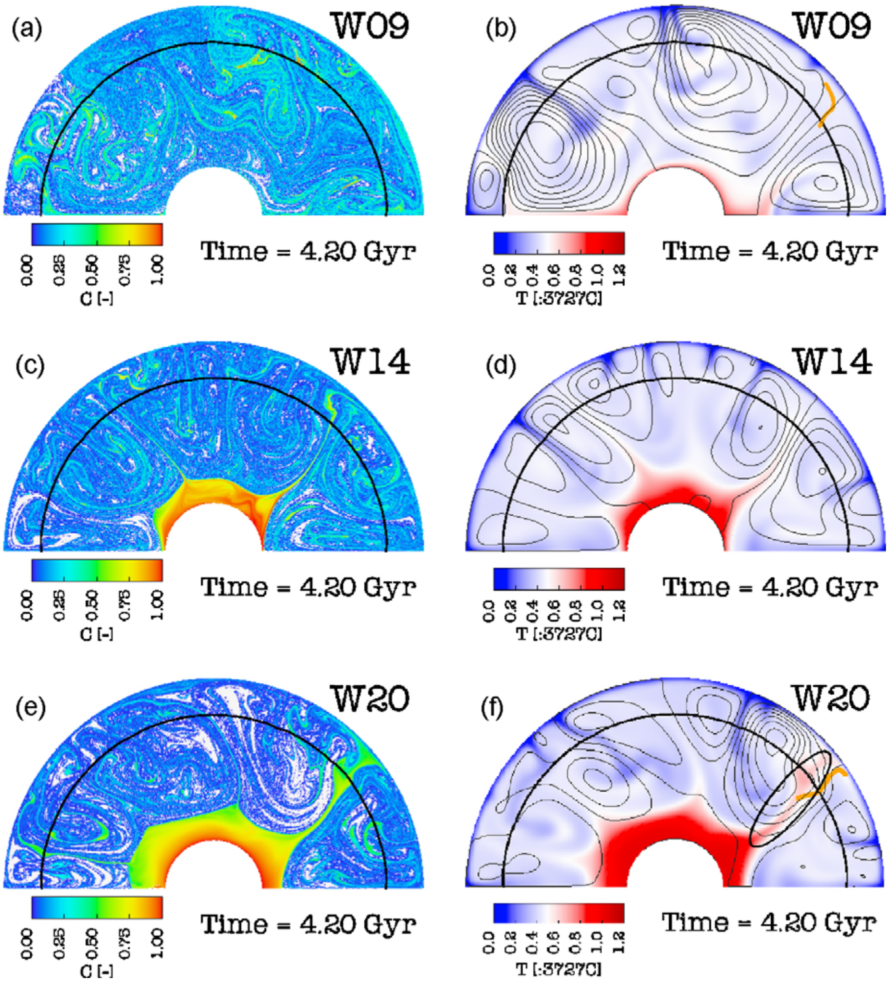

Fig. 2. Similar as Fig. 1 for models (a and b) W09 ($(\delta\rho_C/\rho_0) = 0.9\%$), (c and d) W14 ($(\delta\rho_C/\rho_0) = 1.4\%$), and (e and f) W20 ($(\delta\rho_C/\rho_0) = 2.0\%$). The Clapeyron slope equals $\gamma = -1.25\,\mathrm{MPa\,K^{-1}}$. The elliptic region in frame (f) indicates a deep-seated upwelling that is crossing the phase boundary. The orange line in frames (b) and (f) indicate the monitor tracer paths for which the monitored temperature is shown in Fig. 8 b and c, respectively. (For interpretation of the references to colour in this figure legend, the reader is referred to the web version of the article.)

be filtered from the upwelling convective flow (Weinstein, 1992). In line with the above, the contrast of the composition parameter near 660 km depth (frames c and f) increases for models with increasing excess density of the compositionally distinct material.

In model H10 the radiogenic heat productivity is increased by a factor 10 in the compositionally distinct material, but it is otherwise similar to model S14 (see Table 2). The increased heat productivity results in higher temperatures in the deep reservoir, which decreases its stability. We quantified the trade-off between excess heat productivity and excess density using results from previous numerical modelling experiments (Van Thienen et al., 2005). Since viscosity is temperature-dependent, hot (weak) upwellings are less capable of penetrating the upper mantle (Nakakuki et al., 1994). As a result of the increased convective layering, a larger temperature contrast forms across the phase transition as is shown by the curves for models S14 and H10 in Fig. 5 b and c.

3.2. *Compositional heterogeneity of upwellings*

The models presented above are similar to mantle evolution scenarios proposed by e.g. Kellogg et al. (1999), Becker et al. (1999), Tackley (2002), and Tan and Gurnis (2007) to satisfy a range of geochemical and geophysical constraints. Our models include different degrees of stability of a deep mantle reservoir and convective layering at the transition zone. Heterogeneous material from the lower mantle has been considered as a source of chemical diversity in OIB. To investigate the viability of this mechanism quantitatively for the models discussed above, we examine the amount of heterogeneous material, included in lower mantle material crossing the phase boundary. To this end we apply the monitor tracer diagnostic described in Section 2.1. Results are shown in Fig. 6.

Transport of heterogeneous material should be considered along with the total transport, M_{tot}, which is shown in the top row of Fig. 6. As expected, the rate of total mass transport is larger (factor 2–3) in models where the phase barrier is weak (dashed curves) than in models with a strong phase barrier (solid curves). This is observed for both the rate of inflow into the region enclosing the phase transformation defined in Section 2.1($M_{\mathrm{tot}}^{\mathrm{lm}}$, green curves) as well as the outflow ($M_{\mathrm{tot}}^{\mathrm{um}}$, red curves). The small difference between the inflow and outflow results from the fraction of upwelling material that fails to reach the upper mantle and is returned to the lower mantle. Furthermore, mass transport is promoted during events of downwelling that sink into the lower mantle. This is illustrated by the large transport rates (Fig. 6 a–c) coinciding with high flow velocities of downwelling events (Fig. 3). Transport rates of compositionally distinct material, M_{het}, are depicted in the middle row of Fig. 6. Similar to the total mass transport shown in Fig. 6 a–c, transport rates of heterogeneous material are small in models with a strong

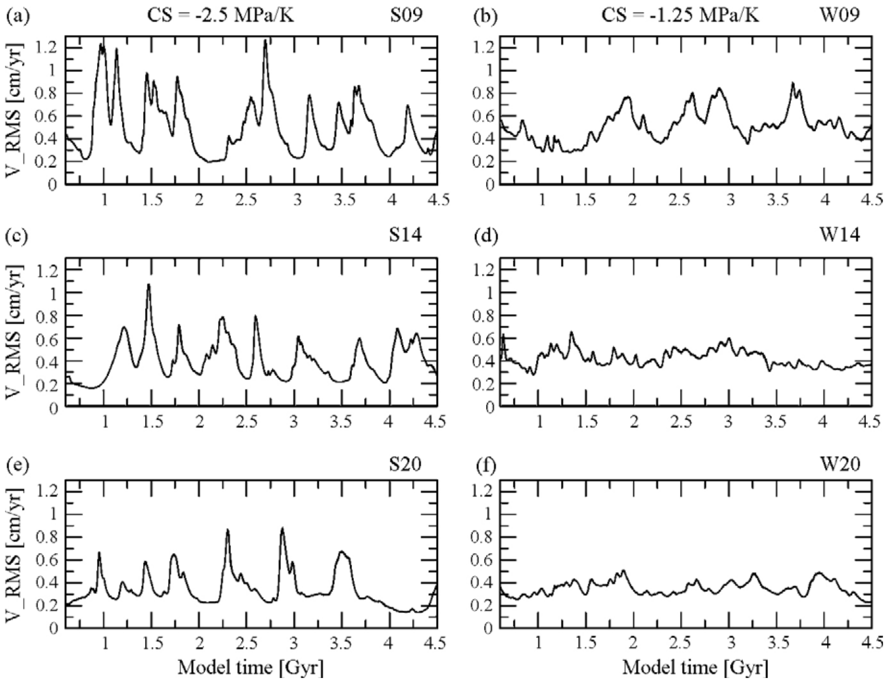

Fig. 3. Time series of the RMS convective flow velocity V_{RMS} for models (a) S09, (b) W09, (c) S14, (d) W14, (e) S20, and (f) W20.

convective layering and show a time dependence that corresponds to the vigour of convection.

A measure that is closely related to petrologic observations is the fraction of heterogeneous material contained in upwellings of lower mantle origin, $f_{\mathrm{het}} = (M_{\mathrm{het}}/M_{\mathrm{tot}})$. The bottom row of graphs in Fig. 6 shows the resulting time series of f_{het}. In sharp contrast to the behaviour of M_{tot} and M_{het}, the fraction f_{het} does not show a strong dependence on the Clapeyron slope. For material crossing the phase transition, the fractions $f_{\mathrm{het}}^{\mathrm{lm}}$ and $f_{\mathrm{het}}^{\mathrm{um}}$ (green and red curves in Fig. 6 g–i) fluctuate between the values 0.001 and 0.002, especially at model times larger than $t = 2.5$ Gyr. Thus, upwellings entering the upper mantle contain a similar fraction of heterogeneous material, for the different thermo-chemical convection models examined. Therefore, a chemically heterogeneous source region for OIB – associated with lower mantle upwellings – seems feasible for a wide range of thermo-chemical evolution scenarios. A reduction of the fraction of heterogeneous material in upwellings during phase crossing is indicative of chemical filtering that preferentially restricts dense material to the lower mantle (Weinstein, 1992). Fig. 6 d–f shows slightly lower values of $f_{\mathrm{het}}^{\mathrm{um}}$ compared to $f_{\mathrm{het}}^{\mathrm{lm}}$. The ratio between $f_{\mathrm{het}}^{\mathrm{um}}$ to $f_{\mathrm{het}}^{\mathrm{lm}}$, averaged over the entire model evolution has a typical value of 0.85, indicating that around 15% of dense material is removed from upwelling material entering the phase transition zone, as a result of chemical filtering.

We also examine the ability of upwellings to reproduce a compositionally diverse signature that is characteristic for OIB. Fig. 7 shows 2D histograms where the statistical distribution of the composition of material entering the upper mantle through the endothermic phase boundary is presented for time bins of 150 Myr and 10 bins that cover the full composition range. Logarithmic values of the number of monitor tracers that have crossed the phase transition normalised by the total number of monitor tracers are colour coded in the 2D histograms. A sharp decrease in the transport into the upper mantle for material with larger composition values is shown in all histograms in Fig. 7. The reduced transport of material of progressively larger excess density is caused primarily by gravitational stability effects, and to a lesser extent by chemical filtering at the phase transition, as has been discussed in preceeding paragraphs. For the entire composition range, the material transport increases at periods of large material exchange between the upper and the lower mantle (see Fig. 7), that coincide with large values of v_{RMS} (see Fig. 3). Increasing $\delta\rho_C/\rho_0$ increases the gravitational stability of the heterogeneous reservoir in the lower mantle as was clearly illustrated by the composition fields in Figs. 1 and 2. Fig. 7 a, c, and e & b, d, and f

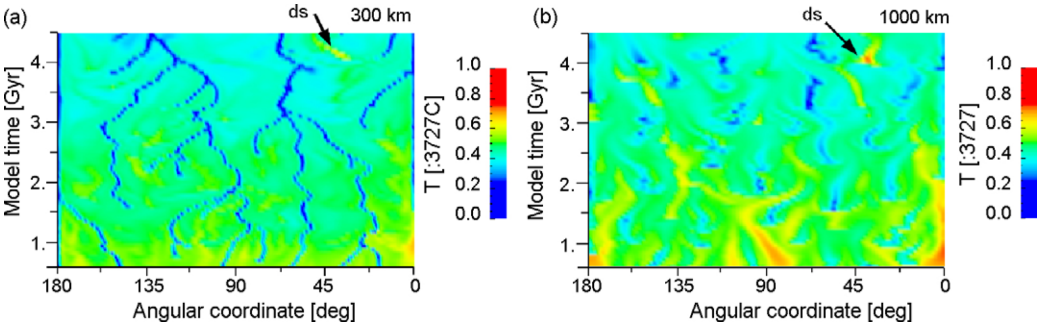

Fig. 4. Dimensionless in situ temperature for model W20 as a function of the angular coordinate (horizontal axis) and model time (vertical axis). The cross-section depth is at (a) 300 km and (b) 1000 km. The arrows labeled 'ds' indicate a deep-seated upwelling.

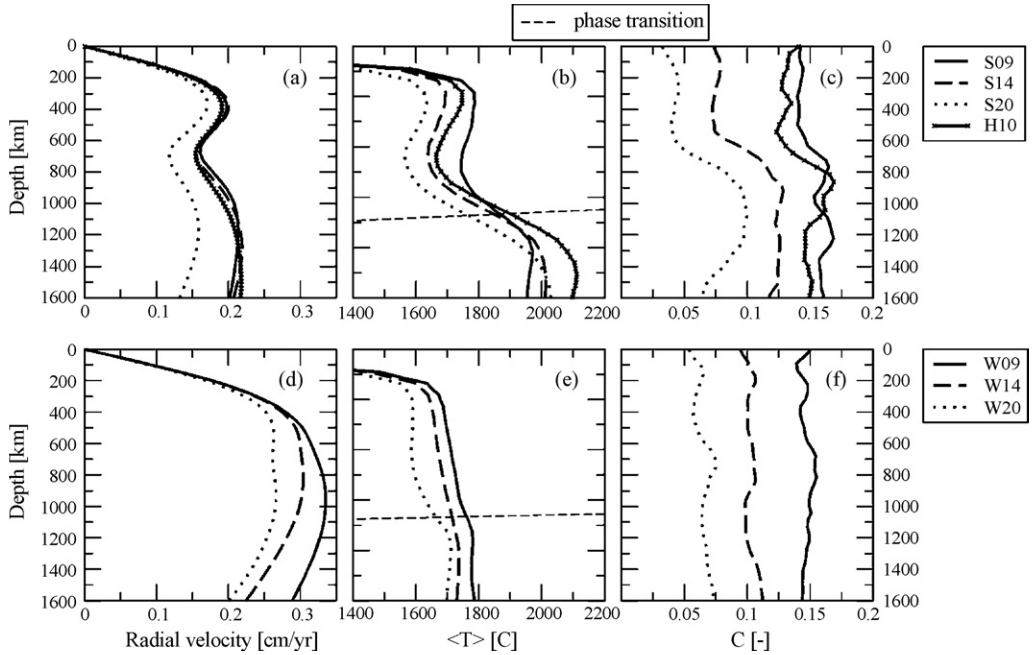

Fig. 5. Depth-profiles averaged over model time 3.0 < *t* < 4.5 Gyr for (a and d) radial convective flow velocity, (b and e) in situ temperature, and (c and f) the composition parameter. Results are shown for models with Clapeyron slope $\gamma = -2.5\,\mathrm{MPa\,K^{-1}}$(top row), and Clapeyron slope $\gamma = -1.25\,\mathrm{MPa\,K^{-1}}$(bottom row), as indicated by the legend. The thin dashed line indicates the Clapeyron slope in our model.

shows models for increasing values of the reservoir excess density; $\delta\rho_C/\rho_0 = 0.9\%$, 1.4%, and 2.0%, respectively. The injection of heterogeneous material into the upper mantle decreases in these models of progressively larger excess density. When increasing the Clapeyron slope from $\gamma = -1.25$ to $-2.5\,\mathrm{MPa\,K^{-1}}$ (right- and left-hand column in Fig. 7, respectively) transport of compositionally distinct material into the upper mantle is reduced. The reduction is caused primarily by a limited total mass exchange between the

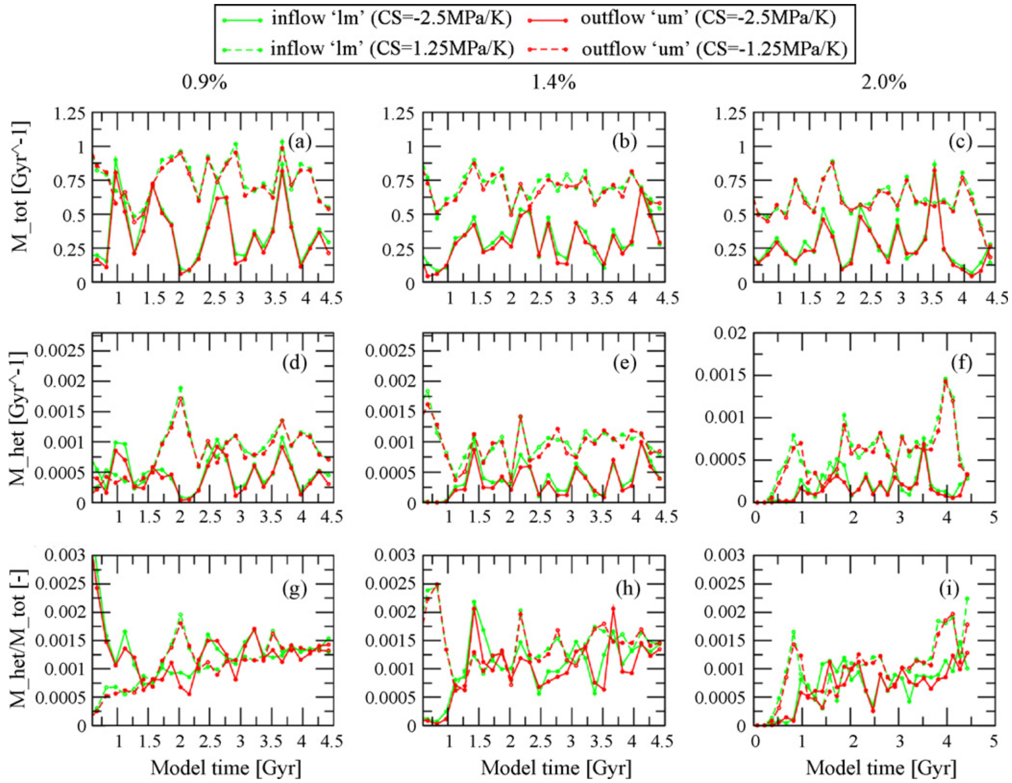

Fig. 6. Time-averaged values of mass fractions plotted at mid-point bin times. (a–c) Total mass transport rate into the upper mantle. (d–f) Heterogeneous mass transport rate into the upper mantle. (g–i) Ratio of heterogeneous to total mass transport into the upper mantle. Solid lines indicate models (a, d, and g) S09, (b, e, and h) S14, and (c, f, and i) S20. The dotted lines indicate models (a, d, and g) W09, (b, e, and h) W14, and (c, f, and i) W20. (For interpretation of the references to colour in this figure legend, the reader is referred to the web version of the article.)

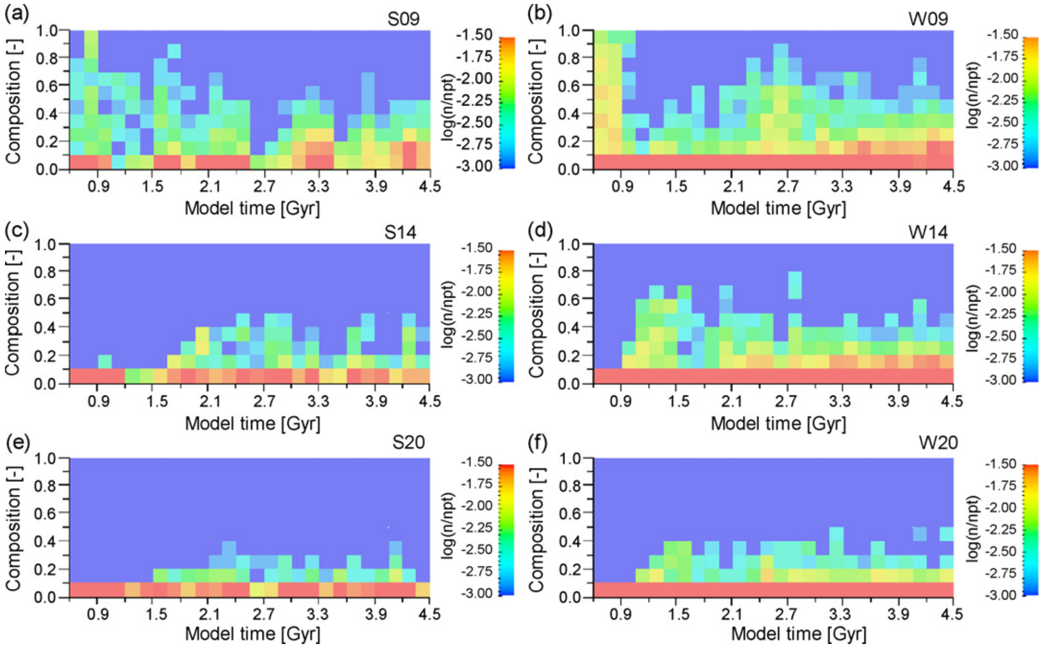

Fig. 7. Histogram of the composition monitored during phase boundary crossing. Plotted is the logarithm of the number of tracer crossings, scaled to the total number of monitor tracers. Logarithmic values are truncated at a minimum value of −3. The model time increases from left to right from 0.6 to 4.5 Gyr, composition increases upwards from 0 to 1. Models shown are (a) S09, (b) W09, (c) S14, (d) W14, (e) S20, and (f) W20. (For interpretation of the references to colour in this figure legend, the reader is referred to the web version of the article.)

upper and lower mantle as was shown by the results presented in Fig. 6.

3.3. Excess temperature of upwellings

To investigate the effect on excess temperatures of the post-spinel phase transition we evaluate the change in excess temperature, denoted T_{ex}, during phase boundary crossings: $\delta T_{\mathrm{ex}} = T_{\mathrm{ex}}^{\mathrm{um}} - T_{\mathrm{ex}}^{\mathrm{lm}}$. Note that positive values of δT_{ex} are associated with an increase in the excess temperature, during phase boundary crossing. Firstly, a temperature contrast across the phase transition results in negative values for $\delta T_{\mathrm{bg}} = T_{\mathrm{bg}}^{\mathrm{um}} - T_{\mathrm{bg}}^{\mathrm{lm}}$ and therefore positive values of δT_{ex}. Secondly, cooling of the ascending tracer during phase boundary crossing results in negative values of $\delta T = T^{\mathrm{um}} - T^{\mathrm{lm}}$, which reduces the excess temperatures.

For a selection of convective upwellings we compare the temperature, T, to the background temperature, T_{bg}. Fig. 8 a shows that a large background temperature contrast of approximately 300 K has developed across the endothermic phase transition for model S09, which has the higher Clapeyron slope magnitude ($\gamma = -2.5$ MPa K^{-1}). A typical example of a temperature-depth trajectory for a passive, mid-mantle upwelling is shown by the black curves in Fig. 8 a, which define the *PTt*-path of a single monitor tracer. In the lower mantle the temperature in the passive upwellings is close to the background temperature (cf. black and red curves below 700 km). As the particle tracer crosses the phase transition, the background temperature contrast between the upper and lower mantle is the main contributor to the excess temperatures of approximately 200 K monitored at 300 km depth (brown line). A comparatively small temperature increase is related to latent heat

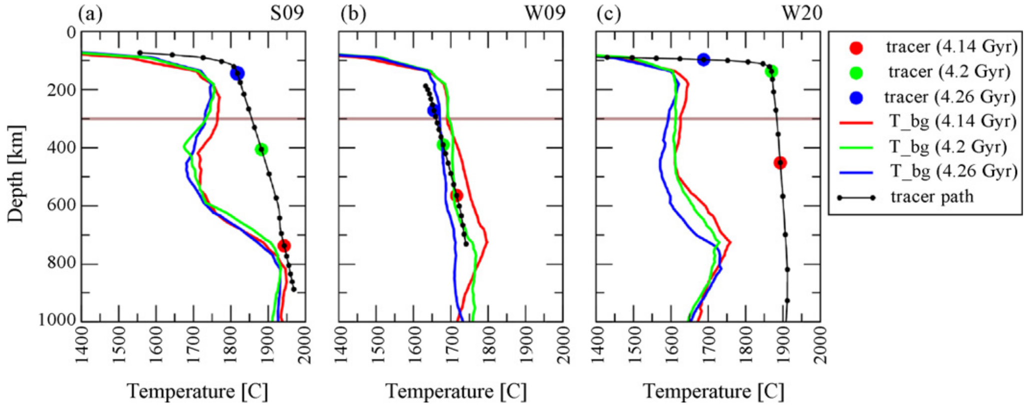

Fig. 8. Red, green, and blue curves show the background temperature, T_{bg} (defined in Section 2.1), for model times $t = 4.14$, 4.2, and 4.26 Gyr, respectively. The black curves show the temperature of monitor tracers crossing the phase transition from below (see the orange curves in Figs. 1 b and h & 2 b and h). Small black dots represent the temperature and depth at equi-distant time intervals of 8 Myr. Coloured thick dots are associated with background temperature profile of corresponding colours. The horizontal brown line indicates the sub-lithospheric monitor depth of 300 km. (For interpretation of the references to colour in this figure legend, the reader is referred to the web version of the article.)

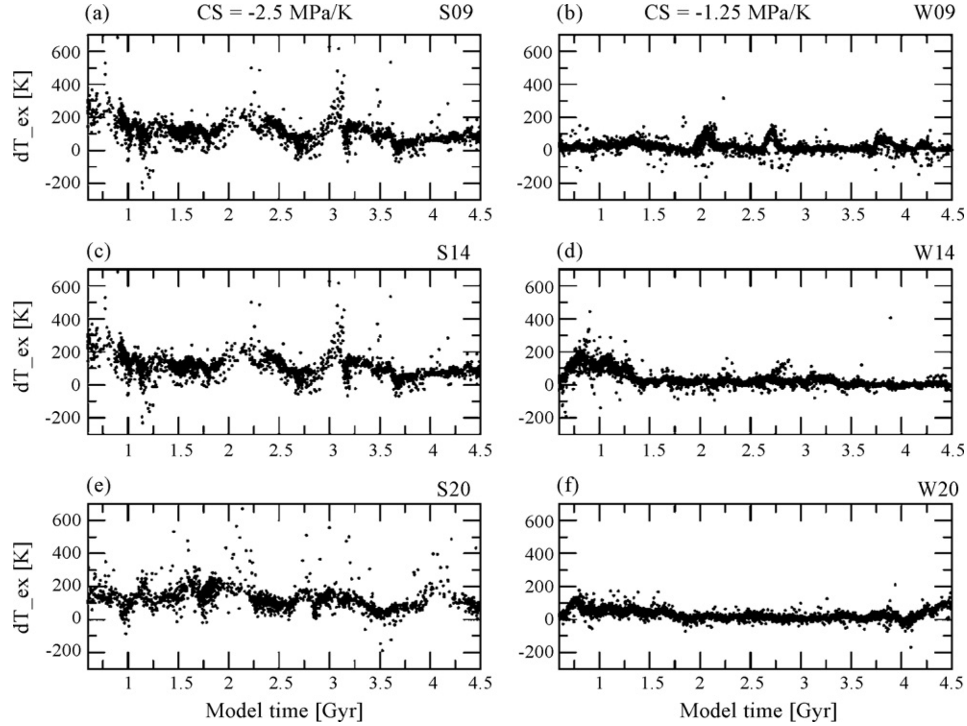

Fig. 9. Time series of δT_{ex}; the change in excess temperatures in upwellings during crossing of the phase transition (see Section 2.1 for definitions). Models shown are (a) S09, (b) W09, (c) S14, (d) W14, (e) S20, and (f) W20.

absorption, which is shown by the small kink in the black curve near 660 km depth.

Fig. 8 shows that the lower Clapeyron slope magnitude ($\gamma = -1.25\,\mathrm{MPa\,K^{-1}}$) produces a small background temperature contrast evolves across the phase transition. The *PTt*-path of the mid-mantle upwelling is close to the background temperature in the lower mantle, similar to the passive upwelling of model S09 in frame a. In this case, the temperature of the upwelling follows the background temperature closely when it enters the upper mantle. The excess temperature monitored at a depth of 300 km is close to 0 K.

The *PTt*-path of an active deep-seated upwelling is clearly different from the passive mid-mantle upwellings (Fig. 8 c) by having a temperature of around 200 K above the background mantle temperature in the lower mantle. Because of its positive thermal buoyancy, the active upwelling ascends faster towards the surface than the passive upwellings, as shown by the larger spacing of the black dots, plotted at equi-distant time intervals of 8 Myr. The high absolute temperature of the deep-seated upwelling is expressed in the high excess temperature around 350 K monitored at 300 km depth, which exceeds geochemically inferred values of 150–300 K.

The above results show that the excess temperature of upwellings increases with the temperature constrast at the phase transition, which in turn increases with the magnitude of the Clapeyron slope. Analysis of the different terms in the energy equation shows that the effects on excess temperature of latent heat production, adiabatic decompression, radiogenic heating, viscous dissipation, and heat diffusion are relatively small. The largest contribution to changes of the in situ temperature is associated with the effect of latent heat. For a 2000 K convective upwelling, the latent heat effect at a Clapeyron slope of $\gamma = -2.5\,\mathrm{MPa\,K^{-1}}$ results in a 89 K temperature increase in the upwelling, which is in agreement with other mantle convection studies (e.g. Christensen, 1998). Half this value is present for the models with a Clapeyron slope of $\gamma = -1.25\,\mathrm{MPa\,K^{-1}}$. As a result, latent heat promotes high excess temperatures in models with a large Clapeyron slope magnitude. Adiabatic cooling is close to 20 K per 100 km for a 2000 K convective upwellings near the depth of the endothermic phase transition. Radiogenic heating results in a temperature increase smaller than 0.2 K per Myr, around a model time of 4.2 Gyr, or less than 2 K during a 100 km rise at a vertical velocity of $1\,\mathrm{cm\,year^{-1}}$. Conductive heat transfer can be neglected: it is many times smaller than convective heat transfer, for an upwelling with a vertical velocity of $1\,\mathrm{cm\,yr^{-1}}$($Pe = 36$, using a length-scale of $h = 100\,\mathrm{km}$). The viscous dissipation was calculated in a 400×400 box surrounding a rising tracer at the moment of phase transition crossing. Typical low values correspond to a heating rate of 1 K per 100 Myr.

The examples shown in Fig. 8 represent the general behaviour of passive and active upwellings in the experiments conducted in this study. Average values over the time interval $3.6 < t < 4.5$ Gyr of δT_{bg}, δT and δT_{ex} are listed in Table 2. A temperature contrast between the upper and lower mantle results in negative values for δT_{bg}, giving a positive contribution to δT_{ex}. This is counteracted by absolute temperatures that decrease during phase crossing (i.e. negative δT). For weak convective layering ($\gamma = -1.25\,\mathrm{MPa\,K^{-1}}$), δT_{bg} is slightly larger in magnitude than δT, which results in a modest rise of excess temperatures. For strong convective layering ($\gamma = -2.5\,\mathrm{MPa\,K^{-1}}$), however, the large increase of excess temperatures δT_{ex} is controlled by a decrease in the background mantle temperature T_{bg}, and the relative contribution of the absolute temperature effect δT is small.

The influence of the phase transition on the excess temperature of mantle upwellings during model evolution is shown in Fig. 9. Values for δT_{ex} up to 400 K are reached in models with Clapeyron slope $\gamma = -2.5\ \mathrm{MPa\,K^{-1}}$. The pronounced temporal fluctuations result from the intermittent style of mantle convection; during periods of layered mantle convection the temperature contrast across the phase change increases, which promotes large values of δT_{ex}. These periods correspond to the low mantle flow velocities shown in Fig. 3 a, c, and e. The behaviour of excess temperature is notably different in models with Clapeyron slope $\gamma = -1.25\,\mathrm{MPa\,K^{-1}}$. In absence of

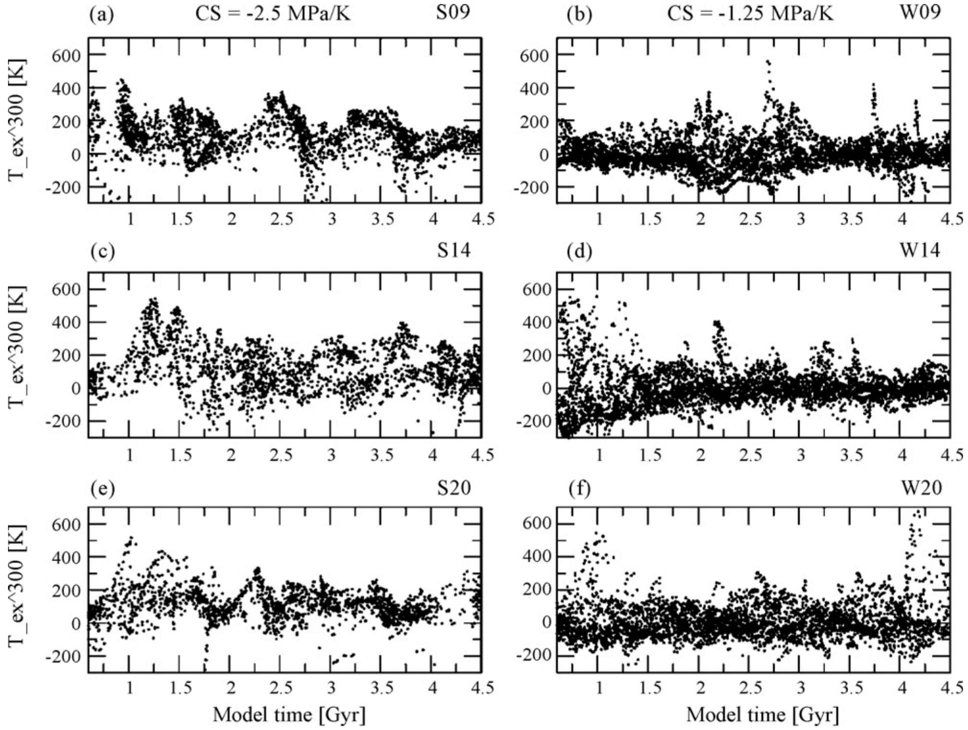

Fig. 10. Time series of the excess temperature T_{ex} at a sub-lithospheric depth of 300 km (see Section 2.1 for definitions). Models shown are (a) S09, (b) W09, (c) S14, (d) W14, (e) S20, and (f) W20.

strong convective layering, a less pronounced temperature contrast across the phase transition develops, compared to the case with $\gamma = -2.5\,\mathrm{MPa\,K^{-1}}$. As a consequence, a modest increase in excess temperature during phase boundary crossing occurs in the models with the weaker Clapeyron slope ($\gamma = -1.25\,\mathrm{MPa\,K^{-1}}$). This is shown in Fig. 9 b, d, and f where the bulk of upwelling material is characterised by δT_{bg} values below 100 K. The smaller values of δT_{bg} listed in Table 2 further illustrate this effect.

Next, we examine the excess temperature of upwellings that have crossed the phase boundary and approach the zone of partial melting acting as the source region of intra-plate volcanism. Fig. 10 shows time series of the excess temperatures monitored at a sub-lithospheric depth of 300 km. In models with Clapeyron slope $\gamma = -1.25\,\mathrm{MPa\,K^{-1}}$ (right-hand column of Fig. 10) the excess temperature in the upwellings is generally less than 300 K — values that are consistent with geochemical estimates of 150–300 K excess temperature extrapolated along a mantle adiabat to surface pressure (e.g. Putirka et al., 2007; Herzberg et al., 2007). Infrequently, however, deep-seated upwellings (see Fig. 2b) produce large excess temperatures with peak values as large as $T_{\mathrm{ex}} = 500\,\mathrm{K}$. Clearest examples are shown in Fig. 10 for model W09 around model times of $t = 2.7$, 3.7 and 4.2 Gyr, for model W14 (Fig. 10d) at $t = 2.2$ and 3.5 Gyr, and model W20 (Fig. 10f) at $t = 4.2$ Gyr. For the deep-seated upwellings, large excess temperatures result from high absolute temperatures in the upwellings (Fig. 8c). Models with Clapeyron slope $\gamma = -2.5\,\mathrm{MPa\,K^{-1}}$, shown in the left-hand column of Fig. 10, show large values of T_{ex}, up to 500 K. These values are substantially larger than the geochemically inferred values. For the models with the larger Clapeyron slope magnitude, the maxima of excess temperatures monitored at 300 km depth only fall within the range of geochemically inferred excess temperatures for the model with neutral compositional excess density (model S00, Table 2). This is explained by excess temperatures that increase with the compositional excess density, which promotes the convective layering, as was shown in Fig. 5.

4. Discussion

Endothermic phase transitions – such as the post-spinel phase transition incorporated in our models – promote layering of the convective flow (e.g. Tackley, 1995) and produces a temperature constrast across the phase boundary (e.g. Christensen and Yuen, 1985). We have shown that, as a consequence of this temperature contrast, the excess temperature increases in upwellings upon crossing of the phase transition. Analysis of the energy equations shows that – during phase boundary crossing – the excess temperature in upwellings is controlled by the background temperature.

At a Rayleigh number of 4×10^6 and a Clapeyron slope of $-2.5\,\mathrm{MPa\,K^{-1}}$, the effective phase buoyancy parameter $P_{\mathrm{e}} = -0.18$ is close to the critical value of $P = -0.25$ estimated by e.g. Christensen and Yuen (1985), Machetel and Weber (1991), and Nakakuki et al. (1994). The occurence of intermittent, partial layering in our models is in agreement with those studies. Partial layering at the transition zone is in line with seismological data, that indicate a varying degree of connectivity of seismic velocities across the mantle transition zone for different study regions (e.g. Van der Hilst et al., 1991; Van der Hilst and Seno, 1993; Fukao et al., 1999; Nataf, 2000; Lei and Zhao, 2006; Zhao, 2007). The temperature contrast that develops between the upper and lower mantle (around 400 K for a Clapeyron slope of $\gamma = -2.5\,\mathrm{MPa\,K^{-1}}$) is in agreement with previous modelling studies (e.g. Tackley et al., 1993).

In general, both the strength of the thermal boundary in the phase transformation region and the excess temperature increases with increasing magnitude of the Clapeyron slope. In the models with a Clapeyron slope value of $\gamma = -1.25\,\mathrm{MPa\,K^{-1}}$ the contribution of convective layering to excess temperatures is around 100 K. For these models, upwellings of lower mantle origin measured at a sub-lithospheric depth of 300 km have maximum excess temperatures that fall in the range of geochemically inferred values of 150–300 K for the potential temperature extrapolated adiabatically to surface pressure (e.g. Schilling, 1991; Putirka et al., 2007;

Herzberg et al., 2007). The infrequent occurence of deep-seated upwellings that enter the upper mantle with excess temperatures as large as 500 K could be associated with the formation of LIPs, because high excess temperatures promote the generation of large volume flood basalt eruptions (Farnetani and Richards, 1994). Furthermore, a deep mantle origin from a heterogeneous reservoir has been proposed for LIPs (e.g. Torsvik et al., 2006). A convection regime with low degrees of layering at the transition zone, therefore, provides an interesting possibility for generating LIPs that coexist with hotspots.

A Clapeyron slope of $-2.5\,\mathrm{MPa\,K^{-1}}$, which produces stronger convective layering, yields excess temperatures that are larger than the 150–300 K inferred from OIB geochemistry (e.g Schilling, 1991; Putirka et al., 2007; Herzberg et al., 2007). The difference between model predictions and geochemically inferred values of excess temperature cannot be explained by heat diffusion, adiabatic decompression, or entrainment of (colder) surrounding material (Farnetani and Richards, 1994). For upwellings with such high excess temperatures, the formation of massive vigourous surface eruption events is expected.

Thus, our modelling suggests that excess temperatures are consistent with geochemically inferred values when the transition zone acts as a weak barrier to convective flow. At larger degrees of layering, lower mantle upwellings may continuously generate flood basalt events — a scenario that is less realistic for the present-day Earth. The residense of hot, intrinsically dense material underneath the phase transition promotes convective layering and, consequently, higher excess temperatures. Therefore, the Clapeyron slope magnitude must be smaller for thermo-chemical mantle convection than for iso-chemical convection to produce excess temperature values that are consistent with inferences from mantle petrology.

The 4% larger excess temperatures that result from evaluating temperatures at 300 km depth instead of extrapolating the temperatures adiabatically to the surface (see Section 2.1) is small, compared to the magnitude of calculated values and, therefore, does not change the conclusions of our study. The background temperatures extrapolated adiabatically to the surface from a sub-lithospheric depth of 300 km is around 1500 K after 4.5 Gyr model time. We realise that this value is on the high side compared to petrological estimates of the mantle potential temperature in the range 1300–1450 K (e.g. McKenzie and Bickle, 1988; Green and Falloon, 1998; Putirka et al., 2007). With additional control experiments, we verified the validity of the results by showing the small influence of the initial potential temperature on the diagnosed excess temperature and chemical heterogeneity in upwellings.

In the models, the compositionally distinct material contained in mantle upwellings results from a heterogeneous reservoir, initially placed in the lower mantle. Evidence for a compositionally heterogeneous lowermost mantle comes from seismological observations (Van der Hilst and Kárason, 1999; Ishii and Tromp, 1999; Saltzer et al., 2004; Deschamps et al., 2007), and geochemical contraints (Hofmann, 1997). A compositionally distinct mantle reservoir can accumulate from the (combined) addition of eclogite-rich material subducted or delaminated from the lithosphere (Christensen and Hofmann, 1994; Van Thienen et al., 2004; Tolstikhin et al., 2006), iron-rich products from the core (Jeanloz and Lay, 1993; Mao et al., 2006), and remnants of magma ocean solidification in the early Earth (e.g. Abe, 1996).

Our model results suggest that different combinations of convective flow layering and reservoir configurations can produce upwellings that transport similar fractions of compositionally distinct material to the upper mantle. Apparently, the chemically heterogeneous signature of OIB (e.g. Hofmann, 1997) is feasible for a wide range of evolutionary mantle models, including possible scenarios where the deep mantle reservoir is configured as a continuous layer (e.g. Kellogg et al., 1999), isolated piles on top of the CMB (Tackley, 2002), or stretched-out blobs dispersed throughout the mantle (Becker et al., 1999). Several modelling studies have shown the feasibility of reproducing the chemical signature of OIB in distinct mantle reservoirs (e.g. Christensen and Hofmann, 1994; Samuel and Farnetani, 2003; Xie and Tackley, 2004, ?). Our results show that a heterogeneous compositional expression in upwellings of lower mantle origin is a robust feature of thermo-chemical mantle convection. We have demonstrated that the densest fractions of a compositionally distinct reservoir are retained in the lower mantle due to gravitational stability and to a smaller extent by chemical filtering at the phase transition. The reservoir can serve as a complement for Earth's heat budget and resolve apparant conflicts in isotope systematics (Kellogg et al., 1999; Albarede and Van der Hilst, 2002; Tolstikhin et al., 2006).

5. Conclusions

We have performed numerical modelling experiments to study the impact of convective layering at the transition zone on transport of compositionally heterogeneous material from the deep lower mantle into the upper mantle. We compared the excess temperatures produced by models with phase transitions of different strength with estimates from geochemical analysis of intra-plate volcanism. We tested a range of long-term thermo-chemical evolution scenarios that have been proposed as possible mantle models (e.g. Kellogg et al., 1999; Becker et al., 1999; Tackley, 2002) by modelling compositionally distinct reservoirs of different stability conditions. The main conclusions are the following.

(i) An increase of excess temperatures in upwellings that enter the upper mantle results from the temperature constrast across the post-spinel phase transition, induced by regional and transient convective layering. When upwellings cross the phase transition, a 400 K increase in excess temperatures occurs during periods of partially layered mantle convection, in models with a Clapeyron slope value of $\gamma = -2.5\,\mathrm{MPa\,K^{-1}}$.

(ii) At low degrees of mantle flow layering, values for the excess temperatures of upwellings are consistent with the combined existence of hotspots and LIPs. In contrast, a strong degree of convective layering promotes upwellings of high excess temperatures that can produce massive flood basalt volumes. Such a scenario is not consistent with data from present-day intraplate volcanism at the Earth's surface. Because hot, intrinsically dense material below the phase transition favours a high degree of convective layering, thermo-chemical convection implies a smaller Clapeyron slope (for the excess temperature to be consistent with OIB analysis) than iso-chemical convection.

(iii) For a range of thermo-chemical mantle convection scenarios, heterogeneous material transport in upwellings of lower mantle origin towards the surface provides a mechanism to generate a chemically heterogeneous signature of OIB for a wide range of stability conditions for the deep mantle.

Acknowledgements

We acknowledge thorough and constructive reviews from Takashi Nakagawa, Teresa Lassak and an anonymous reviewer, which greatly helped to improve the manuscript. This work has been supported by the Dutch National Science Foundation (NWO) under grant VICI 865.03.001. Computational resources for this work were provided by the Netherlands Research Center for Integrated

Solid Earth Science (ISES 3.2.5 High End Scientific Computation Resources).

References

Abe, Y., 1996. Thermal and chemical evolution of the terrestrial magma ocean. Earth Planet. Sci. Lett. 100, 27–39.

Albarede, F., Van der Hilst, R.D., 2002. Zoned mantle convection. Philos. Trans. R. Soc. Lond. A 360, 2569–2592.

Anderson, D.L., 2006. Speculations on the nature and cause of mantle heterogeneity. Tectonophysics 416, 7–22.

Becker, T.W., Kellogg, J.B., O'Connell, R.J., 1999. Thermal constraints on the survival of primitive blobs in the lower mantle. Earth Planet. Sci. Lett. 171, 351–365.

Boehler, R., 2000. High-pressure experiments and the phase diagram of lower mantle and core materials. Rev. Geophys. 38, 221–245.

Bijwaard, H., Spakman, W., 1999. Tomographic evidence for a narrow whole mantle plume below Iceland. Earth Planet. Sci. Lett. 166, 121–126.

Bunge, H.-P., 2005. Low plume excess temperatures and high core heat flux infer red from non-adiabatic geotherms in internally heated mantle circulation models. Phys. Earth Planet. Int. 153, 3–10.

Campbell, I.H., 2007. Testing the plume theory. Chem. Geol. 24, 126–153.

Castle, J.C., Van der Hilst, R.D., 2003. Searching for seismic scattering off mantle interfaces between 800 km and 2000 km depth. J. Geophys. Res. 108 (B2), 2095.

Christensen, U.R., Hofmann, A.W., 1994. Segregation of subducted oceanic crust in the convecting mantle. J. Geophys. Res. 99 (B10), 19,867–19884,19884.

Christensen, U.R., 1989. Models of mantle convection: one or several layers. Philos. Trans. R. Soc. Lond. A 328, 417–424.

Christensen, U.R., Yuen, D.A., 1984. The interaction of a subducting lithospheric slab with a chemical or phase boundary. J. Geophys. Res. 89 (B6), 4389–4402.

Christensen, U.R., Yuen, D.A., 1985. Layered convection induced by phase transitions. J. Geophys. Res. 90 (B12), 10291–10300.

Christensen, U.R., 1998. Dynamic phase boundary topography by latent heat effects. Earth Planet. Sci. Lett. 154, 295–306.

Chopelas, A., Boehler, R., 1992. Thermal expansivity in the lower mantle. Geophys. Res. Lett. 19 (19), 1983–1986.

Cserepes, L., Yuen, D.A., 2000. On the possibility of a second kind of mantle plume. Earth Planet. Sci. Lett. 183, 61–71.

Davies, G.F., 1986. Mantle convection under simulated plates: effects of heating modes and ridge and trench migration, and implications for the core–mantle boundary, bathymetry, the geoid and Benioff zones. Geophys. J. Roy. Astron. Soc. 84, 153–183.

Deschamps, F., Trampert, J., Tackley, P.J., 2007. Thermo-chemical structure of the lower mantle: seismological evidence and geodynamical consequences. In: Yuen, D.A., Maruyama, S., Karato, S.I., Windley, B.F. (Eds.), Superplume: Beyond Plate Tectonics. Springer, pp. 293–320.

Dziewonski, D.L., Anderson, D.L., 1981. Preliminary reference Earth model. Phys. Earth Planet. Int. 25, 297–356.

Farnetani, C.G., 1997. Excess temperatures of mantle plumes: the role of chemical stratification across D. Geophys. Res. Lett. 24 (13), 1583.

Farnetani, C.G., Richards, M.A., 1994. Numerical investigations of the mantle plume initiation model for flood basalt events. J. Geophys. Res. 99 (B7), 13,813–13833,13833.

Fei, Y., van Orman, J., Li, J., van Westrenen, W., Sanloup, C., Minarik, W., Hirose, K., Kombayashi, T., Walter, M., 2004. Experimentally determined postspinel transformation boundary in Mg_2SiO_4using MgO as an internal pressure standard and its geophysical implications. J. Geophys. Res. 109, B02305.

Fischer, K.M., Jordan, T.H., Creager, K.C., 1988. Seismic constraints on the morphology of deep slabs. J. Geophys. Res. 93, 4773–4783.

Fukao, Y., Widiyantoro, S., Obayashi, M., 1999. Stagnant slabs in the upper and lower mantle transition region. Rev. Geophys. 39 (3), 291–323.

Green, D.H., Falloon, T.J., 1998. Pyrolite: a ringwood concept and its current expression. In: Jackson, I. (Ed.), The Earth's Mantle, pp. 311–378.

Hansen, U., Yuen, D.A., Kroenings, S.E., Larsen, T.B., 1993. Dynamic consequences of depth-dependent thermal expansivity and viscosity on mantle circulations and thermal structure. Phys. Earth Planet. Int. 77 (3–4), 205–223.

Hansen, U., Yuen, D.A., 2000. Extended-Boussinesq thermal–chemical convection with moving heat sources and variable viscosity. Earth Planet. Sci. Lett. 176, 401–411.

Herzberg, C., Asimow, P.D., Arndt, N., Niu, Y., Lesher, C.M., Fitton, J.G., Cheadle, M.J., 2007. Temperatures in ambient mantle and plumes: constraints from basalts, picrites, and komatiites. Geochem. Geophys. Geosyst. 8, Q02006.

Hirose, K., 2002. Phase transitions in pyrolitic mantle around 670-km depth: implications for upwelling plumes from the lower mantle. J. Geophys. Res. 107 (B4).

Hockney, R.W., Eastwood, J.W., 1988. Computer simulation using particles. Institute of Physics Publishing Ltd., Bristol.

Hofmann, A.W., 1997. Mantle geochemistry: the message from oceanic volcanism. Nature 385, 219–229.

Irifune, T., Ringwood, A.E., 1993. Phase transformations in subducted oceanic crust and buoyancy relationships at depths of 600–800 km in the mantle. Earth Planet. Sci. Lett. 117, 101–110.

Ishii, M., Tromp, J., 1999. Normal-mode and free-air gravity constraints on lateral variations in velocity and density of Earth's mantle. Science 285, 1231–1236.

Ita, J., King, S.D., 1994. Sensitivity of convection with an endothermic phase change to the form of governing equations, initial conditions, boundary conditions, and equation of state. J. Geophys. Res. 99, 15919–15938.

Ito, E., Takahashi, E., 1989. Postspinel transformations in the system Mg_2SiO_4 and some geophysical implications. J. Geophys. 94 (B8), 10637–10646.

Jacobs, M.H.G., de Jong, B.H.W.S., 2007. Placing constraints on phase equilibria and thermophysical properties in the system $MgO\text{-}SiO_2$ by a thermodynamically consistent vibrational method. Geochim. Cosmochim. Acta 71, 3630–3655.

Jeanloz, R., Lay, T., 1993. The core–mantle boundary. Sci. Am. 268 (5), 48–55.

Jeanloz, R., Morris, S., 1987. Is the mantle geotherm sub-adiabatic? Geophys. Res. Lett. 14, 335–338.

Kellogg, J.B., Jacobsen, S.B., O'Connell, R.J., 2007. Modeling lead isotopic heterogeneity in mid-ocean ridge basalts. Earth Planet. Sci. Lett. 262 (3–4), 328–342.

Kellogg, L.H., 1991. Interaction of plumes with a compositional boundary at 670 km. Geophys. Res. Lett. 18, 865–868.

Kellogg, L.H., Hager, B.H., Van der Hilst, R.D., 1999. Compositional stratification in the deep mantle. Science 283, 1881–1884.

Lei, J., Zhao, D., 2006. A new insight into the Hawaiian plume. Earth Planet. Sci. Lett. 241, 438–453.

Machetel, P., Weber, P., 1991. Intermittent layered convection in a model mantle with an endothermic phase-change at 670 km. Nature 350, 55–57.

Mambole, A., Fleitout, L., 2002. Petrological layering induced by an endothermic phase transition in the Earth's mantle. Geophys. Res. Lett. 29 (22), 2044.

Mao, W.L., Mao, H., Sturbahn, W., Zhao, J., Prakapenka, V.B., Meng, Y., Shu, J., Fei, Y., Hemley, R.J., 2006. Iron-rich post-perovskite and the origin of ultralow-velocity zones. Science 312, 564–565.

McKenzie, D., Bickle, M.J., 1988. The volume and composition of melt generated by extension of the lithosphere. Journal of Petrology 29 (3), 625–679.

Morgan, W.J., 1971. Convecting plumes in the lower mantle. Nature 230, 42.

Nakagawa, T., Buffett, B.A., 2005. Mass transport mechanism between the upper and lower mantle in numerical simulations of thermochemical mantle convection with multicomponent phase changes. Earth Planet. Sci. Lett. 230 (1–2), 11–27.

Nakagawa, T., Tackley, P.J., 2004. Thermo-chemical structure in the mantle arising from a three-component convective system and implications for geochemistry. Phys. Earth Planet. Int. 146, 125–138.

Nakakuki, T., Sato, H., Fujimoto, H., 1994. Interaction of the upwelling with the phase and chemical b oundary at the 670 km discontinuity: effects of temperature-dependent viscosity. Earth Planet. Sci. Lett. 121, 369–384.

Nataf, H., 2000. Seismic imaging of mantle plumes. Annu. Rev. Earth. Planet. Sci. 28, 391–417.

Nolet, G., Allen, R., Zhao, D., 2007. Mantle plume tomography. Chem. Geol. 241, 248–263.

Nolet, G., Karato, S., Montelli, R., 2006. Plume fluxes from seismic tomography. Earth Planet. Sci. Lett. 248, 685–699.

Olson, P., Yuen, D.A., 1982. Thermochemical plumes and mantle phase transitions. J. Geophys. Res. 87 (B5), 3993–4002.

Ono, S., Ito, E., Katsura, T., 2001. Mineralogy of subducted basaltic crust (MORB) from 25 to 37 GPa, and chemical heterogeneity of the lower mantle. Earth Planet. Sci. Lett. 190, 57–63.

Putirka, K.D., Perfit, M., Ryerson, F.J., Jackson, M.G., 2007. Ambient and excess mantle temperatures, olivine thermometry, and active vs. passive upwelling. Chem. Geol. 241, 177–206.

Ribe, N.M., Stutzmann, E., Ren, Y., van der Hilst, R., 2007. Buckling instabilities of subducted lithosphere beneath the transition zone. Earth Planet. Sci. Lett. 254, 173–179.

Saltzer, R.L., Stutzmann, E., Van der Hilst, R.D., 2004. Poisson's ratio in the lower mantle beneath Alaska: evidence for compositional heterogeneity. J. Geophys. Res. 109, B06301.

Saltzer, R.L., van der Hilst, R.D., Karason, H., 2001. Comparing P and S wave heterogeneity in the mantle. Geophys. Res. Lett. 28 (7), 1335–1338.

Samuel, H., Farnetani, C.G., 2003. Thermochemical convection and helium concentrations in mantle plumes. Earth Planet. Sci. Lett. 207, 39–56.

Schilling, J., 1991. Fluxes and excess temperatures of mantle plumes inferred from their interaction with migrating mid-ocean ridges. Nature 352, 397–403.

Segal, A., Praagman, N. P., 2000. The SEPRAN package. Technical report. http://ta.twi.tudelft.nl/sepran/sepran.html.

Solheim, L.P., Peltier, W.R., 1993. Mantle phase transitions and layered convection. Can. J. Earth Sci. 30 (5), 881–892.

Steinbach, V., Hansen, U., Ebel, A., 1989. Compressible convection in the Earth's mantle: a comparison of different approaches. Geophys. Res. Lett. 16 (7), 633–636.

Steinbach, V., Yuen, D.A., 1994. Effects of depth-dependent properties on the thermal anomalies produced in flush instabilities from phase-transitions. Phys. Earth Planet. Int. 86 (1–3), 185–203.

Steinbach, V., Yuen, D.A., 1995. The effects of temperature-dependent viscosity on mantle convection with the two major phase transitions. Phys. Earth Planet. Int. 90, 13–36.

Steinbach, V., Yuen, D.A., Zhao, W., 1993. Instabilities from phase transistions and the timescales of mantle thermal evolution. Geophys. Res. Lett. 20 (12), 1119–1122.

Tackley, P.J., 1995. On the penetration of an endothermic phase transition by upwellings and downwellings. J. Geophys. Int. 100 (B8), 15477–15488.

Tackley, P.J., 2002. Strong heterogeneity caused by deep mantle layering. Geochem. Geophys. Geosyst. 3 (4).

Tackley, P.J., Stevenson, D.J., Glatzmaier, G.A., Schubert, G., 1993. Effects of an endothermic phase transition at 670 km depth in a spherical model of convection in the Earth's mantle. Nature 361, 699–704.

Tan, E., Gurnis, M., 2007. Compressible thermochemical convection and application to lower mantle structures. J. Geophys. Res. 112, B06304.

Tolstikhin, I.N., Hofmann, A.W., 2005. Early crust on top of the Earth's core. Phys. Earth Planet. Int. 148, 109–130.

Tolstikhin, I.N., Kramers, J.D., Hofmann, A.W., 2006. A chemical Earth model with whole mantle convection: the importance of a core–mantle boundary layer (D”) and its early formation. Chem. Geol. 226, 79–99.

Torsvik, T.H., Smethurst, M.A., Burke, K., Steinberger, B., 2006. Large igneous provinces generated from the margins of of the large low-velocity provinces in the deep mantle. Geophys. J. Int. 167, 1447–1460.

Trampert, J., van der Hilst, R. D., 2005. Towards a quantitative interpretation of global seismic tomography. In: Van der Hilst, R.D., Bass, J., Trampert, J. (Eds.), Earth's Deep Mantle: Structure, Composition, and Evolution. AGU Geophysical Monograph, vol. 160. pp. 47–62.

Turcotte, D.L., Schubert, G., 2002. Mantle Dynamics. Cambridge University Press.

Van den Berg, A.P., Rainey, E.S.G., Yuen, D.A., 2005. The combined influences of variable thermal conductivity, temperature- and pressure-dependent viscosity and core–mantle coupling on thermal evolution. Phys. Earth Planet. Int. 149, 259–278.

Van den Berg, A.P., Van Keken, P.E., Yuen, D.A., 1993. The effects of a composite non-Newtonian and Newtonian rheology on mantle convection. Geophys. J. Int. 115, 62–78.

Van der Hilst, R.D., Widiyantoro, S., Engdahl, E.R., 1997. Evidence for deep mantle circulation from global tomography. Nature 386, 578–584.

Van der Hilst, R.D., Kárason, K., 1999. Compositional heterogeneity in the bottom 1000 kilometers of the Earth's mantle: toward a hybrid convection model. Science 283, 1885–1888.

Van der Hilst, R.D., De Hoop, M.V., Wang, P., Shim, S.-H., Tenorio, L., Ma, P., 2007. Seismo-stratigraphy and thermal structure of Earth's core–mantle boundary region. Science 315, 1813–1817.

Van der Hilst, R.D., Seno, T., 1993. Effects of relative plate motion on the deep structure and penetration depth of slabs below the Izu-Bonin and Mariana island arcs. Earth Planet. Sci. Lett. 120, 375–407.

Van der Hilst, R., Engdahl, R., Spakman, W., Nolet, G., 1991. Tomographic imaging of subducted lithosphere below Pacific island arcs. Nature 353, 37–43.

Van Keken, P., 2001. Cylindrical scaling for dynamical cooling models of the Earth. Phys. Earth Planet. Int. 124, 119–130.

Van Keken, P.E., Karato, S., Yuen, D.A., 1996. Rheological control of oceanic crust separation in the transition zone. Geophys. Res. Lett. 23 (14), 1821–1824.

Van Thienen, P., Van den Berg, A.P., Vlaar, N.J., 2004. Production and recycling of oceanic crust in the early Earth. Tectonophysics 386, 41–65.

Van Thienen, P., Van Summeren, J., Van der Hilst, R. D., Van den Berg, A. P., Vlaar, N. J., 2005. Numerical study of the origin and stability of chemically distinct reservoirs deep in Earth's mantle. In: Van der Hilst, R.D., Bass, J., Trampert, J. (Eds.), Earth's Deep Mantle: Structure, Composition, and Evolution. AGU Geophysical Monograph, vol. 160. pp. 117–136.

Weidner, D.J., Wang, Y., 1998. Chemical- and Clapeyron-induces buoyancy at the 660 km discontinuity. J. Geophys. Res. 103 (B4), 7431–7441.

Weinstein, S.A., 1992. Induced compositional layering in a convecting fluid layer by an endothermic phase transition. Earth Planet. Sci. Lett. 113 (1–2), 23–39.

Xie, S., Tackley, P.J., 2004. Evolution of helium and argon isotopes in a convecting mantle. Phys. Earth Planet. Int. 146 (3–4), 417–439.

Xie, S., Tackley, P.J., 2004. Evolution of U–Pb and Sm–Nd systems in numerical models of mantle convection and plate tectonics. J. Geophys. Res. 109, B11204.

Zhao, D., 2007. Seismic images under 60 hotspots: search for mantle plumes. Gondwana Res. 12, 335–355.

Zhong, S., 2006. Constraints on thermochemical convection of the mantle from plume heat flux, plume excess temperature, and upper mantle temperature. J. Geophys. Res. 111, B04409.